

Supershear tsunamis and insights from the M_w 7.5 Palu earthquake

Faisal Amlani,¹ Harsha S. Bhat,² Wim J. F. Simons,³ Alexandre Schubnel,² Christophe Vigny,² Ares J. Rosakis⁴, Joni Efendi⁵, Ahmed Elbanna⁶ and Hasanuddin Z. Abidin⁵

1. *Department of Aerospace and Mechanical Engineering, University of Southern California, Los Angeles, USA.*
2. *Laboratoire de Géologie, École Normale Supérieure, CNRS-UMR 8538, PSL Research University, Paris, France.*
3. *Faculty of Aerospace Engineering, Delft University of Technology, Delft, Netherlands.*
4. *Graduate Aerospace Laboratories, California Institute of Technology, Pasadena, California, USA.*
5. *BIG (Bandang Informasi Geospasial / Geospatial Information Agency), Java, Indonesia.*
6. *Department of Civil and Environmental Engineering, University of Illinois at Urbana Champaign, USA.*

Devastating tsunamis are known to predominantly occur due to subduction zone earthquakes such as the 2011 M_w 9.0 Tohoku-Oki earthquake in Japan. However, the 2018 M_w 7.5 Palu, Sulawesi (Indonesia) strike-slip earthquake generated an unexpected tsunami with disastrous and deadly effects. Since such strike-slip earthquakes are not known to generate large tsunamis, the latter's origin remains much debated. Here we present near-field observational evidence that the earthquake attained supershear speed, i.e., a rupture speed greater than the shear wave speed of the host medium. We study the effect of this rupture phenomenon on generation of tsunamis by coupling the corresponding ground motion to a 1D non-linear shallow water wave model that accounts for both the time-dependent bathymetric displacement as well as, importantly, the bathymetric velocity. Using the local bathymetric profile of Palu bay around the Pantoloan harbour tidal gauge, our simulations clearly reproduce the motions of the observed tsunami with minimal tuning of parameters. This implies that Mach fronts, generated by a supershear earthquake, interacted with the Palu bay to cause the tsunami. Our results suggest that the speed of the rupture should also be included in the assessment of tsunami hazard.

Tsunamis are well-known to be amongst the most destructive consequences of earthquakes,¹⁻⁴ and the 2018 Sulawesi earthquake was no exception: it generated a devastating tsunami^{5,6} in the nearby Palu bay in which hundreds were killed and tens of thousands more displaced from their homes (ASEAN Situation Update No.15 - Earthquake & Tsunami Sulawesi). However, this was an unexpected event since the earthquake was associated with the predominantly in-plane ground motion produced by strike-slip ruptures. As these motions are not known to excite significant waves, the underlying physical mechanisms behind the tsunami have largely remained a mystery⁷. Many studies conducted to explain the phenomenon have not arrived at definitive conclusions⁸ nor have adequately captured tidal gauge records;^{9,10} the main consensus appears to be that some form of ground motion (e.g., landslides¹¹ or the reverse-slip motion of the fault¹²), amplified by the bay, is to blame.

However, a key notable feature of this earthquake is that it ruptured at supershear speed,^{13,14} which results in a manifestation of two shock (or Mach) fronts carrying significant vertical velocity with relatively slow attenuation over large distances.¹⁵ The existence of supershear earthquakes has been proven theoretically and experimentally since the early 1970s.¹⁶⁻²² The M_w 6.5 Imperial Valley earthquake (California, 1979) was the first naturally observed supershear earthquake rupture.²³ Since then, many more (although rare) earthquakes have been recorded to propagate at supershear speeds: the M_w 7.4 1999 Izmit in Turkey,²⁴ the M_w 7.8 2001 Kunlun²⁵ and the M_w 7.8 2002 Denali,^{26,27} to name a few.

Although the overall tsunami behaviour at Palu is likely a combination of several effects that include these supershear dynamics as well as landslides, recent studies^{9,28,29} suggest that the influence from phenomena such as the latter may be secondary: the rupture itself may have created adequate seafloor

movement to excite the tsunami, which was subsequently amplified by the shallow and narrow 2D/3D geometric features of the Palu bay. Jamelot et al.⁹ capture amplitudes recorded by the Pantoloan tidal gauge, but not the first phases and motions—ultimately conceding that a dynamic study should be conducted to better understand the influence of supershear. The model-based study of Ulrich et al.,²⁹ which incorporates some dynamics of supershear in the form of time-dependent ground displacement, better captures tidal gauge records but, again, there remains a mismatch in the first phases and arrival.

Hence the primary objective of this work is to provide the missing link in explaining these discrepancies and more fully understand the role played by supershear rupture dynamics on the generation of the Palu tsunami. In particular, we incorporate a neglected feature in the above-cited works that is a defining characteristic of supershear earthquakes: the *velocity* of the ground motion.¹⁵ Using a model validated by the first near-field evidence of supershear at Palu, our results imply that ground speeds, which better represent the intricacies of the Mach fronts, may further explain the observed motions of the tsunami. Since other studies (including those investigating landslides and liquefaction) have adequately captured much of the observed run-up amplitudes and some local inundations, the scope of this paper is to focus on the first phases and arrival in the Pantoloan records.

Evidence of a supershear rupture

The most unmistakable signature of a supershear rupture is that the fault parallel particle velocity dominates over the fault normal velocity^{27,30} (when the rupture velocity v is greater than $\sqrt{2}c_s$ for a shear wave speed c_s). The opposite signature is expected for a subshear rupture. Fig. 1a shows the Palu-Koro fault system along with the location of the high-rate, 1Hz, PALP GPS station. Figs. 1b-c show the particle velocities recorded during the Sulawesi earthquake, clearly demonstrating a fault parallel particle velocity greater than the fault normal velocity ($\sim 1.0\text{m/s}$ versus $\sim 0.7\text{m/s}$). This proves that the rupture, as it passed by the PALP station, definitively went supershear and hence attained a speed between $\sqrt{2}c_s$ and the P-wave speed, c_p , of the medium (the absolute limiting speed of the rupture). This represents the first-ever observation of a supershear rupture by a high-rate GPS station. Socquet et al.¹⁴ and Bao et al.¹³ have also inferred that this earthquake went supershear, but mainly through far-field observations employing geodetic and teleseismic data, respectively. The only other near-field evidence of a supershear earthquake was obtained using an accelerometer (250Hz) at Pump Station 10 (PS10) during the 2002 Mw 7.9 Denali earthquake.^{26,27}

We can further compare the PALP records against a 3D supershear earthquake simulation¹⁵ whose rupture propagates at a speed of $v = 1.6c_s$ and whose corresponding particle velocities are computed at 100Hz and then decimated to match the 1Hz sampling rate of the GPS observations (see Methods for details). The synthetic data and the GPS records are in excellent agreement for the main rupture pulse (Figs. 1b-c). The subsequent arrivals are not as well-captured since the numerical model does not account for the local velocity structure and the detailed fault geometry. A similar comparison with synthetic velocities computed for a subshear rupture ($v = 0.8c_s$) finds that they are in poor agreement with GPS data (Figs. 1d-e). This clearly suggests that the supershear rupture speed was $1.6c_s$ (around 5.3km/s) when it passed by the PALP GPS station (Ulrich et al.²⁹ also find a speed greater than $\sqrt{2}c_s$). We have thus provided the first near-field high-rate GPS-based evidence that the Sulawesi earthquake rupture actually did go supershear as claimed and, further, have validated the numerical data employed to source the tsunami model in what follows.

Modelling the effect of supershear velocity on tsunami generation

Using the synthetic particle motions (which, again, agree with PALP GPS records and are generated by the 3D supershear earthquake model), a 1D non-linear shallow water wave model incorporating time-dependent bathymetry movements in ground velocity and displacement³¹ has been utilized to simulate

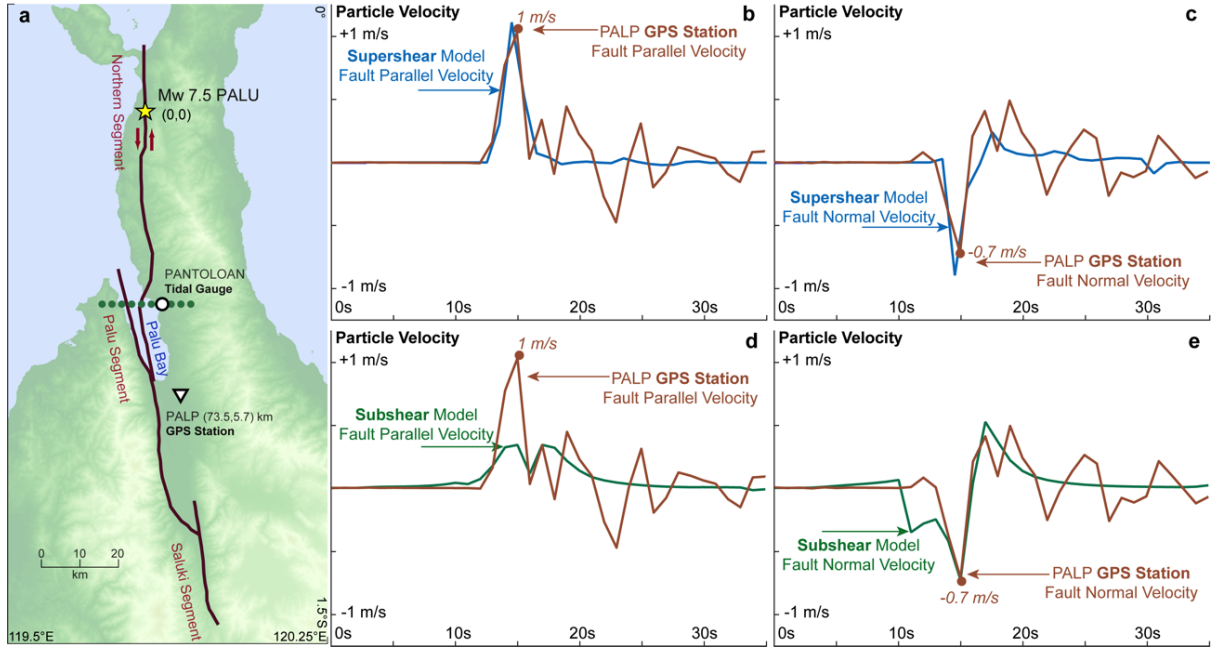


Fig. 1. The earthquake rupture and near-field evidence of supershear. **a**, The Palu-Koro fault system, where the Pantoloan tidal gauge and the PALP GPS station are marked. The green line of dots represents the slice of the bay considered for the tsunami model employed in this study. **b**, Comparison between the fault parallel particle velocities recorded at the PALP station with those generated by the numerical supershear rupture model.¹⁵ **c**, Comparison between the corresponding fault normal particle velocities. **d,e**, Same as **(b,c)** but for a subshear rupture.

the generation and propagation of the tsunami. This employs the depth-averaged shallow water approximation of the Euler equations that can be written as a system of coupled hyperbolic partial differential equations given by

$$\begin{cases} \frac{\partial H}{\partial t} + \frac{\partial(Hu)}{\partial y} = 0 \\ \frac{\partial(Hu)}{\partial t} + \frac{\partial(Hu^2)}{\partial y} + gH \frac{\partial \eta}{\partial y} = 0 \end{cases}, \quad 0 \leq y \leq L, \quad t \geq 0. \quad (1)$$

Here, $u(y, t)$ is the fluid velocity, $\eta(y, t)$ is the sea surface height and $H(y, t) = h_0(y) + h(y, t) + \eta(y, t)$ is the absolute height from the bed-level to the water surface for an initial at-rest bathymetry $h_0(y)$. The entire domain of length L is subjected to a time-dependent ground perturbation $h(y, t)$ which—together with the corresponding ground velocity $\partial h(y, t)/\partial t$ included in system (1)—sources the subsequent tsunami dynamics. In what follows, these values are determined from the 3D supershear earthquake model¹⁵ and illustrated in the seismograms of Fig. 2. The constant g is the acceleration due to gravity.

The specific Palu bay configuration is outlined in Fig. 3a along with the governing equations defined on the horizontal y -axis, where $z = \eta(y, t)$ represents the water height relative to the background sea level. The bathymetry shape closely approximates that of the segment demarcated by the green dotted line near the Pantoloan tidal gauge in Fig. 1a (basin width 9.2km, maximum depth 710m and an average slope of 7° to the east and 27° to the west of the bay). The shallowest part is taken to be 1m, and the distance between the virtual gauge and the fault is 4.3km. The complete computational domain is taken to be twice the basin width ($L = 18.4$ km). Fig. 3b presents a temporal snapshot in the (x, y) -plane (the ground surface) illustrating the dynamic vertical velocity field (and the associated Mach fronts) which is input as a synthetic source in conjunction with its corresponding time-dependent displacement field. The fault and the sense of slip (left-lateral) are indicated in red, and the data applied to perturb the bathymetry is taken along the line demarcated by dark green circles (whose locations correspond to the

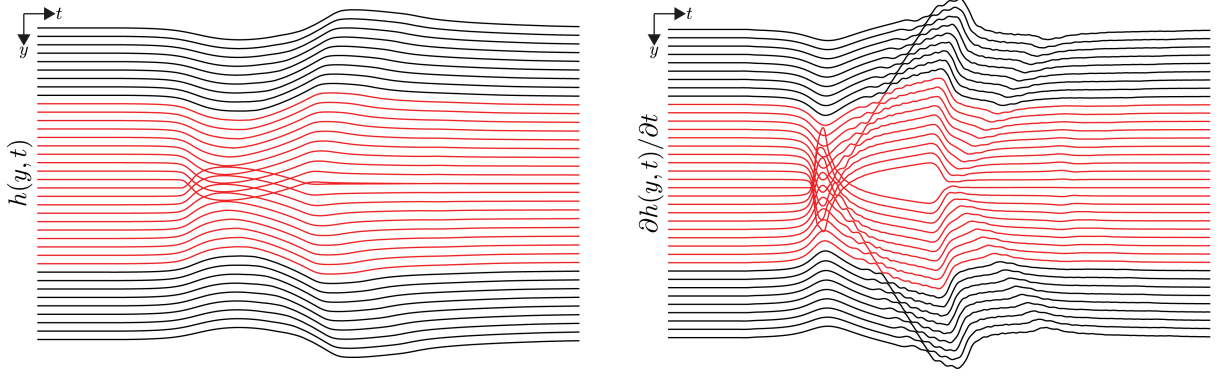


Fig. 2. Dynamic rupture modelling. Representative synthetic particle displacement (left) and velocity (right) histories from Dunham and Bhat.¹⁵ Red lines correspond to the location of the Palu bay.

same markers indicated in the model domain of Fig. 3a). For an example point located at (x_0, y_0) and highlighted in a larger light green circle, the plots of Fig. 3c additionally present the temporal evolution of both the vertical velocity (which can reach $\sim 1\text{m/s}$ along the domain) as well as its corresponding ground displacement (which, in the 1D setting, can reach $\sim 40\text{cm}$). As already noted (and further illustrated in Fig. 2), the shapes and the maximum values of these profiles remain fairly unattenuated at large distances from the original earthquake—a hallmark of the energy carried by supershear shock fronts.¹⁵ For the results that subsequently follow, Figs. 3d-e additionally present the analogous inputs for classical modelling of seismogenic tsunamis. In a classical setting,³² the earthquake source is often modelled as a static displacement perturbation applied to the bathymetry (rather than dynamic ground motion), i.e., a static $h(y, t) = h(y)$ that neither accounts for the time-dependence nor the velocity of the sea floor (other simple approximations to more complicated sources are also standard^{33,34}). From the supershear earthquake results, this corresponds to the final, permanent ground displacement at the end of the temporal profiles in Fig. 3c and is expectedly on the order of a few centimeters.

Capturing first motions and arrival recorded at Pantoloan

Numerical solution of the non-linear shallow water wave equations has been facilitated by a spectral Fourier continuation (FC) methodology^{35,36} employing a bathymetry that closely resembles the Palu bay near the Pantoloan tidal gauge (see Figs. 1,3). Through use of a discrete periodic extension in space and explicit integration in time, such a solver enables high-order accuracy, mild Courant-Friedrichs-Lewy (CFL) constraints on the temporal discretisation and nearly dispersionless resolution of propagating waves over large distances (see Methods). Fig. 4 presents simulation results in the (t, y) -plane (time and space) of the water height $z = \eta(y, t)$ and, more importantly, presents a comparison between observations recorded every minute by the Pantoloan tidal gauge (whose geographic location is indicated in Fig. 1a) with that predicted by the dynamic source model (plotted in Fig. 4 at the same frequency). The numerical modelling has been conducted at a much higher temporal resolution (on the order of 10 milliseconds), and the Pantoloan records have been obtained and processed by the Agency for Geospatial Information (BIG), Indonesia (<http://tides.big.go.id>). Remarkably, both the first motions and phases from the observation records are in excellent agreement with the 1D approximation generated by excitation from the dynamic supershear earthquake. Later phases, which can be attributed to tsunami wave reflections within the Palu bay, are not as well-captured since our model does not fully account for the localised effects of the 2D/3D bathymetric profile. Nevertheless, the tsunami arrival and primary dynamics are correctly reproduced.

For comparison, Fig. 5 presents the corresponding simulations that are classically-sourced by the final (static) vertical displacement given by the same supershear earthquake simulation. Although a

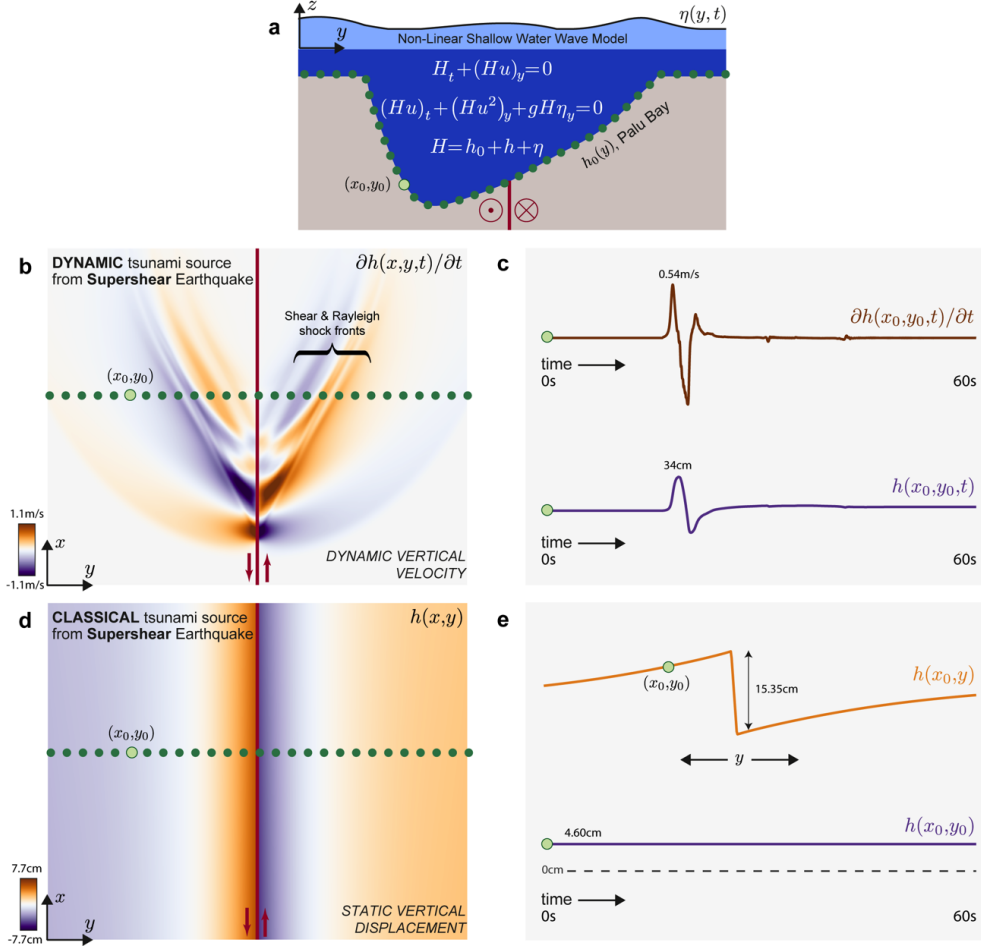


Fig. 3. The non-linear tsunami model setup that incorporates displacement and velocity ground dynamics. The strike-slip fault and its sense of motion are indicated in red in all the panels. **a**, Snapshot of the dynamic vertical velocity from a supershear earthquake with, **b**, its temporal evolution at an example point (x_0, y_0) (light green). **c**, The static displacement field due to a supershear earthquake. **d**, A diagram of the non-linear shallow water wave system for tsunami height η , initial bathymetry h_0 and bathymetry perturbation (source) h . The dark green dots on the supershear earthquake data in **(a,c)** correspond to the source locations used to perturb the bathymetry domain in **(d)**. **e**, The spatial profile in y of the static displacement field due to a supershear earthquake.

tsunami is generated, there are large contrasts in phase, width and particularly the sign (Fig. 5) when compared to the Pantoloan tidal gauge observations. This implies that the complex ground motion (which is not accounted for by classical tsunami models) must be incorporated in order to correctly predict the tsunami dynamics as in Fig. 4. We note that we have normalized water heights by their corresponding maxima for comparison throughout: since more energy is carried *along* the fault¹⁵ running in the direction x (Fig. 3), the 1D model in y will naturally generate lower amplitudes (of the order of half a meter). However, similar tsunami signatures can still be expected and, indeed, Jamelot et al.⁹ incorporated a more comprehensive (classical) model treating localised effects of the 2D/3D bathymetry but generated the same mismatches in phase as those in Fig. 5.

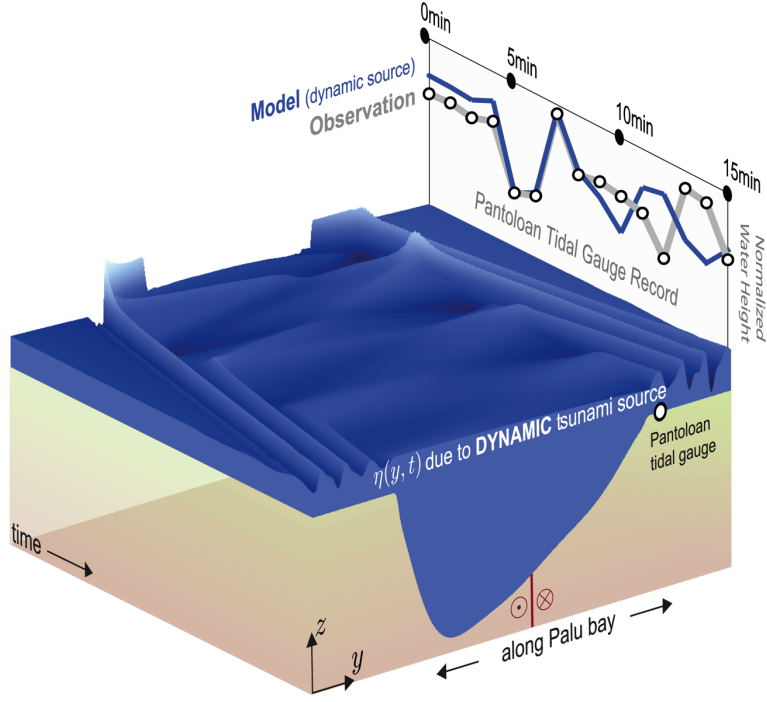


Fig. 4. Simulated tsunami using dynamic ground motion (including velocity). Spatio-temporal evolution $\eta(y, t)$ of the tsunami along the Palu bay due to dynamic bathymetry velocity and displacement from a supershear earthquake. Normalised Pantoloan tidal gauge records during the event are overlaid with model predictions.

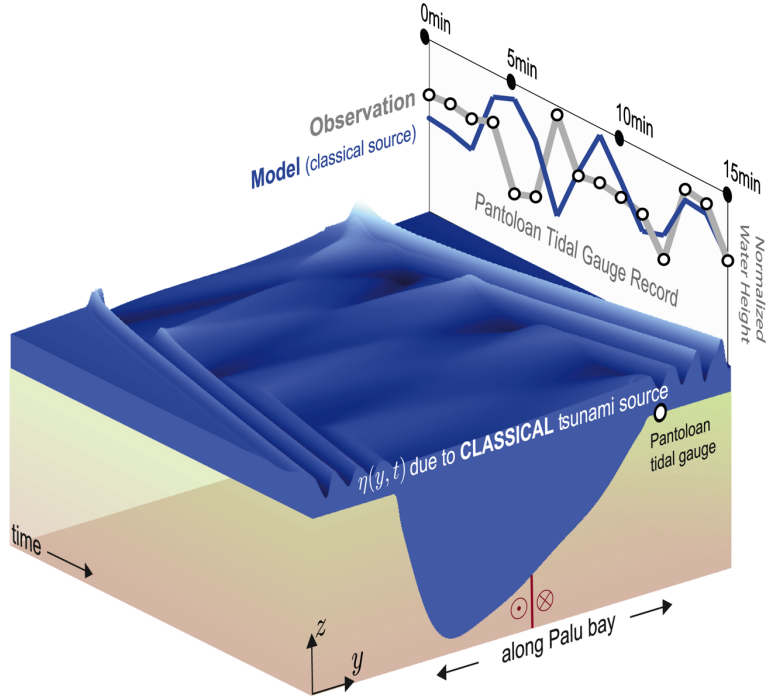


Fig. 5. Simulated tsunami using classical (static) displacement. Spatiotemporal evolution $\eta(y, t)$ of the tsunami along the Palu bay due to static displacement from a supershear earthquake. Normalised Pantoloan tidal gauge records during the event are overlaid with model predictions.

Conclusions

Hence we confirm that the Sulawesi earthquake went supershear via the first near-field high-rate GPS-based evidence of such a rupture and that, by modelling the corresponding effect on the generation of tsunamis in a shallow geometry, we conclude that the ground motion resulting from the associated Mach fronts (which carry minimally attenuated velocities to large distances) may well have caused the Palu tsunami. Since nothing geologically specific about the bay has been introduced, our results signify the importance of such configurations for tsunami hazard assessment due to strike-slip earthquakes. The same physical ingredients (supershear rupture and a shallow bay) may combine to produce similar effects elsewhere, including the Tomales bay in California (which is crossed offshore by the San Andreas fault system³⁷) and the Izmit bay in Turkey (which is crossed by the North Anatolian fault³⁸). Both these regions, as well as the Palu bay, have suffered from historical tsunamis. On the contrary, the 2012 Off Northern Sumatra earthquake and the 2013 Craig, Alaska earthquake both went supershear but caused negligible (or no) tsunamis since they occurred in deep ocean without any shallow bay near them. Additionally, the 1999 Izmit earthquake was subshear as it passed through the Izmit bay and thus generated only a negligible tsunami. Hence we reemphasise that supershear rupture *and* a shallow bay are key to generate significant tsunamis. We thus suggest that any rapid assessment of tsunami hazard after a strike-slip earthquake should also involve a rapid assessment of the earthquake rupture velocity as we have shown that ultimately the focal mechanism, the depth *and the speed of the rupture* all contribute towards the generation of tsunamis.

References

- [1] R bke, B. R. & V tt, A. The tsunami phenomenon. *Prog. Oceanogr.* **159**, 296–322 (2017).
- [2] Pugh, D. & Woodworth, P. *Sea-level science: understanding tides, surges, tsunamis and mean sea-level changes* (Cambridge University Press, 2014).
- [3] Bryant, E. *Tsunami: The Underrated Hazard* (Springer Berlin Heidelberg, 2008).
- [4] Synolakis, C. E. & Okal, E. A. 1992–2002: perspective on a decade of post-tsunami surveys. In *Tsunamis*, 1–29 (Springer, 2005).
- [5] Mai, P. M. Supershear tsunami disaster. *Nat. Geosci.* **12**, 150 (2019).
- [6] Fritz, H. *et al.* Field survey of the 28 September 2018 Sulawesi Tsunami. In *AGU Fall Meeting Abstracts* (2018).
- [7] Syamsidik, Benazir, Umar, M., Margaglio, G. & Fitrayansyah, A. Post-tsunami survey of the 28 September 2018 tsunami near Palu Bay in Central Sulawesi, Indonesia: Impacts and challenges to coastal communities. *Int. J. Disast R. Re.* **38**, 101229 (2019).
- [8] Muhari, A. *et al.* Solving the puzzle of the September 2018 Palu, Indonesia, tsunami mystery: Clues from the tsunami waveform and the initial field survey data. *J. Disaster Res.* **13 Sci. Comm.**, sc20181108 (2018).
- [9] Jamelot, A., Gailler, A., Heinrich, P., Vallage, A. & Champenois, J. Tsunami simulations of the Sulawesi Mw 7.5 Event: Comparison of seismic sources issued from a tsunami warning context versus post-event finite source. *Pure Appl. Geophys.* **176**, 3351–3376 (2019).
- [10] Heidarzadeh, M., Muhari, A. & Wijanarto, A. B. Insights on the source of the 28 September 2018 Sulawesi tsunami, Indonesia based on spectral analyses and numerical simulations. *Pure Appl. Geophys.* **176**, 25–43 (2019).

- [11] Sassa, S. & Takagawa, T. Liquefied gravity flow-induced tsunami: first evidence and comparison from the 2018 Indonesia Sulawesi earthquake and tsunami disasters. *Landslides* **16**, 195–200 (2019).
- [12] He, L., Feng, G., Li, Z., Feng, Z., Gao, H. & Wu, X. Source parameters and slip distribution of the 2018 Mw 7.5 Palu, Indonesia earthquake estimated from space-based geodesy. *Tectonophysics* **772**, 228216 (2019).
- [13] Bao, H. *et al.* Early and persistent supershear rupture of the 2018 magnitude 7.5 Palu earthquake. *Nat. Geosci.* **12**, 200–205 (2019).
- [14] Socquet, A., Hollingsworth, J., Pathier, E. & Bouchon, M. Evidence of supershear during the 2018 magnitude 7.5 Palu earthquake from space geodesy. *Nat. Geosci.* **12**, 192–199 (2019).
- [15] Dunham, E. M. & Bhat, H. S. Attenuation of radiated ground motion and stresses from three-dimensional supershear ruptures. *J. Geophys. Res.* **113**, 1–17 (2008).
- [16] Burridge, R. Admissible speeds for plane-strain self-similar shear cracks with friction but lacking cohesion. *Geophys. J. Roy. Astr. S.* **35**, 439–455 (1973).
- [17] Andrews, D. J. Rupture velocity of plane strain shear cracks. *J. Geophys. Res.* **81**, 5679–5689 (1976).
- [18] Das, S. & Aki, K. A numerical study of two-dimensional spontaneous rupture propagation. *Geophys. J. Roy. Astr. S.* **50**, 643–668 (1977).
- [19] Wu, F. T., Thomson, K. & Kuenzler, H. Stick-slip propagation velocity and seismic source mechanism. *Bull. Seism. Soc. Am.* **62**, 1621–1628 (1972).
- [20] Rosakis, A. J., Samudrala, O. & Coker, D. Cracks faster than the shear wave speed. *Science* **284**, 1337–1340 (1999).
- [21] Xia, K. W., Rosakis, A. J. & Kanamori, H. Laboratory earthquakes: The sub-Rayleigh-to-supershear rupture transition. *Science* **303**, 1859–1861 (2004).
- [22] Passelègue, F. X., Schubnel, A., Nielsen, S., Bhat, H. S. & Madariaga, R. From sub-Rayleigh to supershear ruptures during stick-slip experiments on crustal rocks. *Science* **340**, 1208–1211 (2013).
- [23] Archuleta, R. J. A faulting model for the 1979 Imperial Valley earthquake. *J. Geophys. Res.* **89**, 4559–4586 (1984).
- [24] Bouchon, M. *et al.* How fast is rupture during an earthquake? New insights from the 1999 Turkey earthquakes. *Geophys. Res. Lett.* **28**, 2723–2726 (2001).
- [25] Robinson, D. P., Brough, C. & Das, S. The M_w 7.8, 2001 Kunlunshan earthquake: Extreme rupture speed variability and effect of fault geometry. *J. Geophys. Res.* **111** (2006).
- [26] Ellsworth, W. L. *et al.* Near-field ground motion of the 2002 Denali fault, Alaska, earthquake recorded at pump station 10. *Earthq. Spectra* **20**, 597–615 (2004).
- [27] Mello, M., Bhat, H. S., Rosakis, A. J. & Kanamori, H. Reproducing the supershear portion of the 2002 denali earthquake rupture in laboratory. *Earth Planet. Sc. Lett.* **387**, 89–96 (2014).

- [28] Oral, E., Weng, H. & Ampuero, J. P. Does a damaged-fault zone mitigate the near-field impact of supershear earthquakes?- Application to the 2018 M_W 7.5 Palu, Indonesia, earthquake. *Geophys. Res. Lett.* **47**, e2019GL085649 (2020).
- [29] Ulrich, T. *et al.* Coupled, physics-based modelling reveals earthquake displacements are critical to the 2018 palu, sulawesi tsunami. *Pure Appl. Geophys.* (2019).
- [30] Dunham, E. M. & Archuleta, R. J. Near-source ground motion from steady state dynamic rupture pulses. *Geophys. Res. Lett.* **32** (2005).
- [31] Dutykh, D. & Clamond, D. Modified shallow water equations for significantly varying seabeds. *Appl. Math. Model.* **40**, 9767 – 9787 (2016).
- [32] Pedlosky, J. *Geophysical Fluid Dynamics* (Springer Science & Business Media, 2013).
- [33] Tanioka, Y. & Satake, K. Tsunami generation by horizontal displacement of ocean bottom. *Geophys. Res. Lett.* **23**, 861–864 (1996).
- [34] Kajiura, K. The leading wave of a tsunami. *Bull. Earthquake Res. Inst.* **141**, 535-571 (1963).
- [35] Lyon, M. & Bruno, O. P. High-order unconditionally stable FC-AD solvers for general smooth domains II. Elliptic, parabolic and hyperbolic PDEs; theoretical considerations. *J. Comput. Phys.* **229**, 3358 – 3381 (2010).
- [36] Amlani, F. & Bruno, O. P. An FC-based spectral solver for elastodynamic problems in general three-dimensional domains. *J. Comput. Phys.* **307**, 333 – 354 (2016).
- [37] Johnson, S. Y. & Beeson, J. W. Shallow Structure and Geomorphology along the Offshore Northern San Andreas Fault, Tomales Point to Fort Ross, California. *Seismol. Soc. Am., Bull.* **109**, 833–854 (2019).
- [38] Altinok, Y. *et al.* The tsunami of August 17, 1999 in Izmit bay, Turkey. *Nat. Hazards* **24**, 133–146 (2001).

Corresponding author

Correspondance and requests for materials should be delivered to
Harsha S. Bhat, harsha.bhat@ens.fr

Acknowledgements

F. A. acknowledges Prof. Oscar Bruno at Caltech for inspiring the numerical technique used in this study. A. S. would like to acknowledge the European Research Council grant REALISM (2016-grant 681346). A.J.R. was supported by the Caltech/MCE Big Ideas Fund (BIF). The continued (long-term) operation of the GPS stations in Central Sulawesi, Indonesia data has been co-facilitated by the EU-ASEAN SEAMERGES (2004-2006) and GEO2TECDI-1/2 projects (2009-2013) in cooperation with the Geospatial Information Agency of Indonesia (BIG). The GPS data acquisition and research was also partly funded by grants from the Dutch NWO User Support Programme Space Research (2007-2018). We would like to express our special thanks to the local staff of the Indonesian Meteorology, Climatology, and Geophysical Agency (BMKG) offices in Palu, both for hosting the GPS station and for being available 24/7 to assist us with optimal operation of the GPS equipment. A special thanks to our local survey staff, Bpak Rahman Umar and Urif, for their continued support, including directly after the earthquake for inspecting the GPS stations.

Author contributions

F. A. and H. S. B. designed and conceived the project and conducted numerical modelling studies. W. J. F. S., J. E. and C. V. have maintained the (high-rate) PALP station and obtained all GPS data. W. J. F. S. did the kinematic GPS data analysis. F. A. and H. S. B. wrote the manuscript. All authors contributed to analysis, interpretation and manuscript preparation.

Competing interests

The authors declare no competing interests.

Methods

GPS data. The dual-frequency GPS has been processed using the scientific GIPSY-OASIS II software version 6.4 (Jet Propulsion Laboratory, 2017). The (post-processing) Precise Point Positioning (PPP) method³⁹ was used in kinematic (1s) mode to derive precise absolute coordinates for the PALP station. Precise ephemeris of GPS satellites (non-fiducial style, using high-rate 30s clocks) along with Earth rotation parameters (ERP) in the IGS14 framework⁴⁰ were obtained from the Jet Propulsion Laboratory (JPL). A satellite elevation mask angle of 7 degrees and absolute IGS antenna phase centre corrections were applied. The Vienna tropospheric Mapping Functions (VMF1) was used (in estimating both zenith delay and gradients) and downloaded from the Global Geodetic Observing System website (<http://vmf.geo.tuwien.ac.at/>). The global ocean tide model applied in the GPS data processing was (FES2014b), and the ocean loading parameters were retrieved from the Onsala Space Observatory website (<http://holt.oso.chalmers.se/>). To enhance the coordinate solutions, the daily global wide lane phase bias (wlpb) files from JPL were used to resolve the phase cycle ambiguities.⁴¹ Although each kinematic position has a higher uncertainty and is affected by biases which usually cancel out over long periods of measurements, the instantaneous co-seismic displacements at PALP were much higher than the high-frequency noise of around 1cm and 2 – 3cm for, respectively, the horizontal and vertical positions. Finally the GPS time tags were corrected to UTC time by subtracting 18s. The co-seismic displacement of the station simply follows from epoch-to-epoch coordinate differences. The standard available script was modified to properly weigh the phase/code measurements of the stations and also to output the correlations. The XYZ positions were then converted to the NEU positions along with their formal standard deviations. They are scaled using the WRMS of all the positions up to the time of the earthquake and generally reach a relative precision (3σ) of about 30mm on the horizontal components. The resulting displacement field was then differentiated by computing adaptive linear fits adapted to satisfy an error to fit criteria. The slope of the linear fit then gives the local velocity. The resulting data was then resampled again at 1Hz by linear interpolation.

Supershear earthquake dynamics and rupture modelling. We have used the existing numerical simulations conducted by Dunham and Bhat.¹⁵ Additional details can be found in the cited manuscript. Numerical simulations were conducted using a staggered-grid finite-difference (FD) code⁴² with the fault boundary conditions implemented using the staggered-grid split-node (SGSN) method.⁴³ As the authors had provided non-dimensionalised results we simply dimensionalized their results for the Palu earthquake by using a shear modulus of 30GPa, stress drop of 10MPa and the shear wave speed of 3.5km/s. The depth of the rupture was assumed to be 10km. The resulting particle velocities and displacements are shown in Fig. 2.

Numerical analysis of shallow water wave equations. The complete non-linear system given by (1) is solved using a numerical scheme based on an accelerated Fourier continuation (FC) methodology for accurate Fourier expansions of non-periodic functions.^{35,36,47} Considering an equispaced Cartesian spatial grid on, for example, the unit interval $[0, 1]$ (given by the discrete points $y_i = i/(N - 1), i = 0, \dots, N - 1$), Fourier continuation algorithms append a small number of points to the discretised function values $\eta(y_i), u(y_i)$ in order to form $(1 + d)$ -periodic trigonometric polynomials $\eta_{\text{cont}}(y), u_{\text{cont}}(y)$ that are of the form

$$\eta_{\text{cont}}(y) = \sum_{k=-M}^M a_k e^{\frac{2\pi i k y}{1+d}}, \quad u_{\text{cont}}(y) = \sum_{k=-M}^M b_k e^{\frac{2\pi i k y}{1+d}} \quad (2)$$

and that match the given discrete values of $\eta(y_i), u(y_i)$, i.e., $\eta_{\text{cont}}(y_i) = \eta(y_i), u_{\text{cont}}(y_i) = u(y_i)$ for $i = 0, \dots, N - 1$. Spatial derivatives in equation (1) are then computed by exact term-wise differentiation

of (2) as

$$\begin{aligned}\frac{\partial \eta}{\partial y}(y_i) &= \frac{\partial \eta_{\text{cont}}}{\partial y}(y_i) = \sum_{k=-M}^M \left(\frac{2\pi i k}{1+d} \right) a_k e^{\frac{2\pi i k y_i}{1+d}}, \\ \frac{\partial u}{\partial y}(y_i) &= \frac{\partial u_{\text{cont}}}{\partial y}(y_i) = \sum_{k=-M}^M \left(\frac{2\pi i k}{1+d} \right) b_k e^{\frac{2\pi i k y_i}{1+d}}.\end{aligned}\tag{3}$$

In essence, FC algorithms add a handful of additional values to the original discretized function in order to form a periodic extension in $[1, 1+d]$ that transitions smoothly from $\eta(1)$ back to $\eta(0)$ (similarly for u). The resulting continued functions can be viewed as sets of discrete values of periodic and smooth functions that can be approximated to high-order on slightly larger intervals by a trigonometric polynomial. Once these discrete periodic continuation functions have been constructed, corresponding Fourier coefficients a_k, b_k in equation (2) can be obtained rapidly from applications of the Fast Fourier Transform (FFT). A detailed presentation on accelerated construction of Fourier continuations can be found in, e.g., Amlani and Bruno.³⁶

Employing these discrete continuations in order to evaluate spatial function values and derivatives on the discretised physical domain modelled by equation (1), the algorithm is completed by employing the explicit fourth-order Adams-Bashforth scheme to integrate the corresponding ODEs in time from the given initial conditions $\eta(y_i, t) = u(y_i, t) = 0$ up to a final given time. The final full solver enables high-order accuracy and nearly dispersionless resolution of propagating waves with mild, linear CFL constraints on the temporal discretisation—properties that are important for adequate resolution of the different spatial and temporal scales involved between the supershear source dynamics and the subsequent tsunami dynamics. Both implicit and explicit FC-based PDE solvers have been successfully constructed and utilised for a variety of physical problems including those governed by classical wave and diffusion equations,^{35,44} non-linear Burgers systems,⁴⁵ Euler equations,⁴⁶ compressible Navier-Stokes equations,^{47,48} fluid-structure hemodynamics equations⁴⁹ and 3D elastodynamics equations.³⁶

Code availability

All codes are available upon request to the corresponding author.

Data availability

All relevant data relating to the supershear earthquake modelling and tsunami modelling are available from the authors upon request.

References

- [39] Zumberge, J. F., Heflin, M. B., Jefferson, D. C., Watkins, M. M. & Webb, F. H. Precise point positioning for the efficient and robust analysis of GPS data from large networks. *J. Geophys. Res.* **102**, 5005–5017 (1997).
- [40] Rebischung, P. & Schmid, R. IGS14/igs14.atx: a new framework for the IGS products. vol. AGU Fall Meeting, San Francisco (2016).
- [41] Bertiger, W. *et al.* Single receiver phase ambiguity resolution with GPS data. *J. Geod.* **84**, 327–337 (2010).
- [42] Favreau, P., Campillo, M. & Ionescu, I. R. Initiation of shear instability in three-dimensional elastodynamics. *J. Geophys. Res.* **107**, 2147–2164 (2002).

- [43] Dalguer, L. A. & Day, S. Staggered-grid split-node method for spontaneous rupture simulation. *J. Geophys. Res.* **112**, B02302 (2007).
- [44] Bruno, O. P. & Prieto, A. Spatially dispersionless, unconditionally stable FC-AD solvers for variable-coefficient PDEs. *J. Sci. Comput.* **58**, 1–36 (2014).
- [45] Bruno, O. P. & Jimenez, E. Higher-order linear-time unconditionally stable alternating direction implicit methods for nonlinear convection-diffusion partial differential equation systems. *J. Fluid. Eng.* **136**, 060904 (2014).
- [46] Shahbazi, K., Hesthaven, J. S. & Zhu, X. Multi-dimensional hybrid Fourier continuation - WENO solvers for conservation laws. *J. Comput. Phys.* **253**, 209 – 225 (2013).
- [47] Albin, N. & Bruno, O. P. A spectral FC solver for the compressible Navier-Stokes equations in general domains I: Explicit time-stepping. *J. Comput. Phys.* **230**, 6248 – 6270 (2011).
- [48] Bruno, O. P., Cubillos, M. & Jimenez, E. Higher-order implicit-explicit multi-domain compressible Navier-Stokes solvers. *J. Comput. Phys.* **391**, 322 – 346 (2019).
- [49] Amlani, F. & Pahlevan, N.M. A stable high-order FC-based methodology for hemodynamic wave propagation. *J. Comput. Phys.* **405**, 109130 (2020).